
ELSEVIER

Fluid Dynamics Research 15 (1995) 365–384

FLUID DYNAMICS RESEARCH

Simulation of turbulent dispersion using Weierstrass modes

Michael Stiassnie[1], Avichay Hadad[2], Michael Poreh

Department of Civil Engineering, Technion – Israel Institute of Technology, Haifa 32000, Israel

Received 9 September 1993; Revised 14 October 1994

Abstract

A simple fractal model is proposed for the dispersion of passive scalars in an incompressible homogeneous turbulent flow field. The dispersion process is based on a three-dimensional velocity field which is assumed to be a linear superposition of Taylor–Green vortices with wave numbers and amplitudes as those in a Weierstrass function. The chosen velocity field satisfies the continuity equation as well as Kolmogorov's inertial range power law, and has a fractal dimension D between upper and lower length-scale bounds. A cloud of tracer particles is relased into the flow field and dispersed by the fluid motion, the trajectories are numerically integrated from the velocity field. The puffs which result from this process are used to examine some aspects of turbulent dispersion, through comparisons with integrated concentration wind-tunnel measurements. The agreement between numerical and experimental results indicates the significance of the proposed simulation model.

1. Introduction

A passive scalar, such as concentration or temperature, emitted into a turbulent flow field is diffused by turbulence, without effecting the dynamics of the flow into which it is emitted. The problem of passive scalar dispersion by a turbulent flow is of wide theoretical and practical importance and many efforts to improve its understanding are reported in the literature, see Hunt (1985). In the last few years, fractal analysis has become an important tool in the study of turbulence and turbulent diffusion, a good survey is given by Sreenivasan (1991).

Any simulation of turbulent dispersion is, naturally, based on some simulation of turbulent fluctuations. In Chapter 2 of this paper we develop a model for simulating turbulent fluctuations. This model flow field is based on a superposition of Taylor–Green vortices ("eddies"), it satisfies Kolmogorov's power law spectrum, and has the major (but not all) fractal properties of measured turbulent flows. Somewhat similar approaches were used by Osborne and Caponio (1990), Humphrey et al. (1992), and Fung et al. (1992).

[1] Member of the Minerva Center for Nonlinear Physics of Complex Systems.

[2] Present address: Department of Environmental Sciences The Weitzmann Institute of Science, Rehovot, Israel.

SSDI 0169-5983(94)00046-8

In Chapter 3 we calculate the evolution of a cloud of particles released in the simulated flow field, and study some fractal properties of the evolving puffs.

In Chapter 4 we compare the numerical results with wind tunnel measurements of integrated concentration. The comparison is focused on three different singularity spectra of integrated concentration records. Namely, (i) the multifractal singularity spectrum, (ii) the dissipation singularity spectrum, and (iii) the spectral singularity spectrum. The mathematical formulation of these three spectra and method of calculation are given in detail in the appendix.

The method of calculation is the same in all three cases, but it is applied on different manipulations of the data sets. The multifractal singularity spectrum provides detailed information about the scaling properties of the original data set; in our case mainly measured or computed integrated concentration (IC) time series. The data set for calculating the dissipation singularity spectrum is obtained by forming the series of squares of concentration differences (gradients) assuming that this magnitude reflects the scalar 'dissipation rate'. The latter spectrum resembles the application of the known singularity spectrum (Halsey et al., 1986) to the energy or scalar 'dissipation rate' (Meneveau and Sreenivasan, 1987; Prasad et al., 1988) in fully developed turbulence. In case of the Spectral Singularity Spectrum we first calculate the accumulated power spectrum of the original signal, and then study its fractal properties.

The overall rather good agreement between theory and experiments is reflected in our conclusions given in Chapter 5.

2. Simulating turbulent fluctuations

2.1. Taylor–Green vortices

Following Taylor and Green (1937) and Brachet et al. (1983), we define a generalized Taylor–Green vortex flow

$$\tilde{u}_i = 4\sqrt{2/3}\sin[\phi_0 + 2\pi(i-1)/3]\prod_{j=1}^{3}\cos[\pi\delta_{ij}/2 - k\tilde{x}_j], \quad i = 1,2,3. \tag{2.1}$$

where $\tilde{x}_i$ is a Cartesian coordinate system, and $\tilde{u}_i$ are the velocity components in this system. δ_{ij} is the Kroenecker delta, $2\pi/k$ is the size of a single vortex cell, and ϕ_0 is an arbitrary phase.

The above incompressible flow field satisfies the continuity equation:

$$\sum_{i=1}^{3} \partial\tilde{u}_i/\partial\tilde{x}_i = 0. \tag{2.2}$$

Its average kinetic energy per unit mass is unity, since

$$\frac{1}{2(2\pi/k)^3}\sum_{i=1}^{3}\int\int\int_{0}^{2\pi/k}\tilde{u}_i^2\,\mathrm{d}\tilde{x}_1\,\mathrm{d}\tilde{x}_2\,\mathrm{d}\tilde{x}_3 = 1. \tag{2.3}$$

The flow (2.1) has a three-dimensional periodic cellular structure, bound to the coordinate system $\tilde{x}_i$. If we choose another coordinate system x_i, unrelated to a particular vortex, then we may

rewrite the flow (2.1) in the new system as

$$u_m = 4\sqrt{2/3} \sum_{i=1}^{3} l_{mi} \sin[\phi_0 + 2\pi(i-1)/3] \prod_{j=1}^{3} \cos\left[\pi\delta_{ij}/2 - k \sum_{n=1}^{3} l_{nj} x_n + \phi_j\right], \quad m = 1,2,3. \tag{2.4}$$

where l_{mi} are the direction cosines of the $\tilde{x}_i$ axis relative to the x_m axes.

In addition to ϕ_0, eq. (2.4) has six new arbitrary phases. Three of them (ϕ_1, ϕ_2, ϕ_3) are related to the transition of the coordinates. The other three (ϕ_4, ϕ_5, ϕ_6) are related to the coordinates rotation:

$$\phi_4 = \cos^{-1}(l_{11}), \quad \phi_5 = \cos^{-1}(l_{12}), \quad \phi_6 = \cos^{-1}(l_{21}), \tag{2.5}$$

All other l_{mi} can be calculated when l_{11}, l_{12} and l_{21} are known. In the sequel we present the flow field by a superposition of Taylor–Green vortices. Each of these vortices should be regarded as a single mode in a 'Fourier type' decomposition, and not as a localized coherent vortex structure.

2.2. *Superposition*

Homogeneous and isotropic turbulent fluctuations are related by their energy spectrum $E(k)$, which is the Fourier Transform of the correlation function

$$\frac{E(k)}{4\pi k^2} = \frac{1}{(2\pi)^3} \int_r \frac{1}{2} \left\langle \sum_{m=1}^{3} u_m(\boldsymbol{x}) u_m(\boldsymbol{x} + \boldsymbol{r}) \right\rangle \exp^{(-i\boldsymbol{k}\cdot\boldsymbol{r})} \mathrm{d}\boldsymbol{r}, \tag{2.6}$$

where $\langle\ \rangle$ denotes an ensemble average, see Batchelor (1970).

The total kinetic energy per unit mass of fluid is

$$\frac{1}{2} \left\langle \sum_{m=1}^{3} u_m^2(\boldsymbol{x}) \right\rangle = \int_0^\infty E(k)\, \mathrm{d}k \tag{2.7}$$

Assuming u_m to be a multivariate Gaussian process, we follow the basic ideas of Rice (1954) and suggest to retrieve u_m from the energy spectrum E through the following stochastic integral

$$u_m = 4\sqrt{2/3} \int_0^\infty \sum_{i=1}^{3} l_{mi}(k) \sin[\phi_0(k) + 2\pi(i-1)/3] \times \prod_{j=1}^{3} \cos\left(\pi\delta_{ij}/2 - k \sum_{n=1}^{3} l_{nj}(k) x_n + \phi_j(k)\right) \sqrt{E(k)\,\mathrm{d}k}, \quad m = 1,2,3. \tag{2.8}$$

with $\phi_p(k)$, $p = 0,1 \ldots ,6$ random phase shifts with a rectangular distribution over $(-\pi, \pi)$.

Eq. (2.8) is actually a linear superposition of Taylor–Green vortices with random origins, random spatial direction and random relative amplitudes, with a given spectrum $E(k)$.

This type of stochastic integrals is quite common in the theory of water-waves, and is described in great detail in Kinsman's (1965) book. The randomness, introduced via the phases, is absolutely necessary. It helps to destroy the cellular structure of the motion. More important, without the randomness, integrals with their differential under a square root sign do not converge. The square root results from the fact that energy is proportional to the square of amplitude. Recent studies

suggest that turbulence is slightly non-Gaussian, see Jimenez et al. (1993). The small drawback of the Gaussian nature of the model (2.8) is circumvented by the finite discretization which we introduce in section 2.3.

To complete our simulation, we choose here an $E(k)$ that represents the inertial subrange expression derived by Kolmogorov (1941).

$$E(k) = E_0 k^{-5/3}, \quad k_o < k < k_d. \tag{2.9}$$

It is well known that the dissipation is "located" in the small scales $k > k_d$ and that energy input comes from the instability of the mean flow $U = (U_1, U_2, U_3)$; occurring at finite $k < k_0$. We have chosen Kolmogorov's spectrum (2.9) as a familiar example, which has some theoretical and experimental support.

We also apply Taylor's frozen-turbulence hypothesis which implies that the vortices are carried with the mean flow. This is introduced in (2.8) by: (i) replacing x_n by $(x_n - U_n t)$, where t is time, on the right-hand-side; and (ii) by subtracting U_m from u_m on the left-hand-side of (2.8). If $\sigma_u = UI$ defines the r.m.s of u_m, where I denotes turbulence intensity, then one finds that $\sigma_u = \sqrt{E_0 k_0^{-2/3}}$

We regard the use of the Kolmogorov spectrum (2.9) as an indirect way of "satisfying" the Navier–Stokes equations of motion (at the level of 2nd order statistics). This is the way by which we introduce dynamics into the model.

2.3. *Relation to Weierstrass function*

To grasp the meaning of the integral in (2.8), or to perform any calculations, one has to introduce some form of discretization. A common way is to take $k_s = k_0 + s\Delta k$, $s = 0,1,2\ldots$. It is however rather rewarding to replace the above arithmetic progression by the following geometric series

$$k_s = k_0 \gamma^s, \quad s = 0,1,2, \ldots, \quad \gamma > 1. \tag{2.10}$$

Both discretizations can be made as dense over an interval as required, by letting either $\Delta k \to 0$ or alternatively $\gamma \to 1^+$. For the discretization (2.10):

$$\mathrm{d}k_s = k_s \ \ln\gamma. \tag{2.11}$$

Substituting the above discretization and the spectrum (2.9) into (2.8) yields:

$$u_m = 4\left(\frac{2\ln\gamma}{3}\right)^{1/2} \sigma_u \sum_{S=0}^{\infty} \gamma^{-S/3} \sum_{i=1}^{3} l_{mi}(s) \sin[\phi_0(s) + 2\pi(i-1)/3]$$
$$\times \prod_{j=1}^{3} \cos\left(\pi\delta_{ij}/2 - k_0\gamma^s \sum_{n=1}^{3} l_{nj}(s)x_n + \phi_j(s)\right), \quad m = 1,2,3. \tag{2.12}$$

The s dependence of (2.12) indicates that the graph of each velocity component u_m, $m = 1,2,3$ is a Weierstrass type function of each of the coordinates x_n, $n = 1,2,3$, when the other two coordinates are held fixed. The dimension of these graphs is $D = 5/3$, see Berry and Lewis (1980). Stiassnie, et al. (1991), in their corollary (2.1), show that a series like (2.12) (viewed as a function of one variable) is a fractional Browman motion. Recently Sreenivasan and Juneja (1993) have used fractional Brownian motion as an example in studying the fractal dimension of measured turbulent time series. It is important to emphasize that (2.12) is much more than an ordinary fractional Brownian

motion; since it gives the whole flow field u_1, u_2, u_3 as a function of x_1, x_2, x_3, and satisfies the continuity equation (2.2). Note that (2.12) with $\gamma > 1$ is non-Gaussian; in contrast to (2.8) or (2.12) with $\gamma \to 1$, which are both Gaussian. This difference results from the fact that the Lindeberg condition (See Feller 1971, p. 262), which guarantees the Gaussianity through the central limit theorem in the latter cases, is not satisfied when $\gamma > 1$. The slight deviation from a Gaussian distribution when $\gamma > 1$ is demonstrated in Osborne and Provenzale (1989).

2.4. *Selection of physical parameters*

Eq. (2.12) has four free parameters: k_0, N, γ, σ_u; which one has to quantify. In this section we explain how the numerical values for these parameters were chosen, while aiming to simulate numerically the experimental measurements which we describe in Section 3.3.

The wave length of the largest vortex in the flow field is $2\pi/k_0$; this should be roughly equal to mesh size M of the grid, which generates the turbulence; see Fig. 7. In our experiment $M = 0.076$ m (Poreh et. al., 1993), thus we have set $2\pi/k_0 = 0.1$ m.

The parameter γ is related to the discretization; see Eq. (2.10). Practically it is related to the size of the smallest vortex and to computer resources. If the upper limit in the sum over s in (2.12) is denoted by N (instead of infinity), then the size of the smallest eddy is $2\pi/(k_0 \gamma^N)$. We estimated the dissipation cut off in the experiment to have a typical length scale of 1 mm and hence set $N = 7$ (eight modes) for a simplified cascade in which each eddy is broken into two smaller ones, i.e., $\gamma = 2$; which yields $2\pi/(k_0 \gamma^N) = 0.8$ mm.

In our simulation, we did not include coordinate rotation and set $l_{ij} = \delta_{ij}$. The mean flow velocity in the experiment was $U = 2.4$ m/s; the typical turbulent intensity, which is affected by the porosity of the grid and the downwind location, was estimated to be $I = 2.5\%$, so that $UI = 0.06$ m/s. In our simulations, we have used that same magnitude for σ_u.

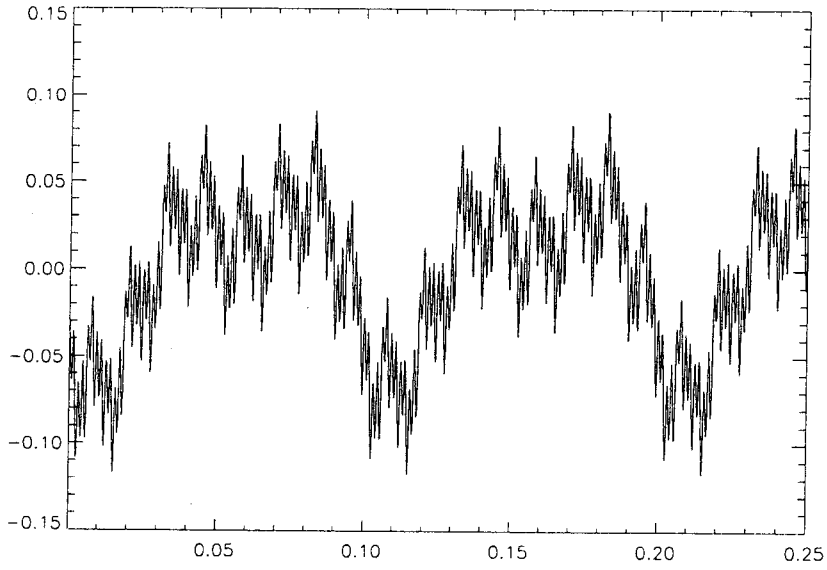

Fig. 1. A typical realization of the fluctuations of a velocity component u_m (vertical axis) as function of time t (horizontal axis) at a fixed point in space for the chosen physical parameters mentioned in Sect. 2.4.

2.5 Fractal properties of the flow

The theoretical flow field (2.12) is a Weierstrass type function with fractal dimension $D = 1.67$. A section of a typical realization of a velocity components is shown in Fig. 1. As a first step one would like to calculate the dimension of this record. The box counting algorithm which is used to calculate the fractal box dimension D_b from such records is given in Appendix A.1. Following Eq. (A.2) Fig. 2a shows the $\log_2$ of number of boxes $N(\delta) = \Sigma_{i=0}^{n-1} \Delta(x_i, \delta)/\delta$ which are needed to cover the record versus $\log_2$ of the size of the box δ. Here all three components of the flow are presented. The straight line corresponds to the range of scales for which the slope (D_b) is calculated. The most left symbol refers to the largest boxes having sides comparable to the size of the mesh size, about 100 mm, whereas the most right symbol refers to small boxes with sides which are related to the Nyquist frequency of the sampling record, about 1.5 mm.

The average box counting dimension of records of the simulated velocity components, using the parameters specified in the previous section, was found to be $D_b = 1.62 \pm 0.1$. Recently Sreenivasan and Juneja (1993) have analyzed turbulent velocity and temperature signals obtained in atmospheric boundary layer over land. They show that these time traces are fractal-like in the classical inertial range of scales, with fractal dimension 1.65 ± 0.05.

Meneveau and Sreenivasan (1987) clearly demonstrate the multifractal nature of the turbulent flow field and calculate $f(\alpha)$, the dissipation singularity spectrum, (see Appendix as well as Fig. 2b). Usually, the $f(\alpha)$ curves have a typical convex structure. Their significant part, near the maximum at α_0 (α_0 is the most probable Lipschitz–Holder exponent) can be approximated by the following single parameter quadratic expression:

$$f(\alpha) = 1 - 0.25(\alpha - \alpha_0)^2/|1 - \alpha_0|. \tag{2.13}$$

The single most important point on the $f(\alpha)$ curve is $\alpha_{M.C.} = 2 - \alpha_0$ where $f(\alpha_{M.C.}) = 1$; here M.C. stands for the measure concentrate. Most of the measure (dissipation) is concentrated on a set of

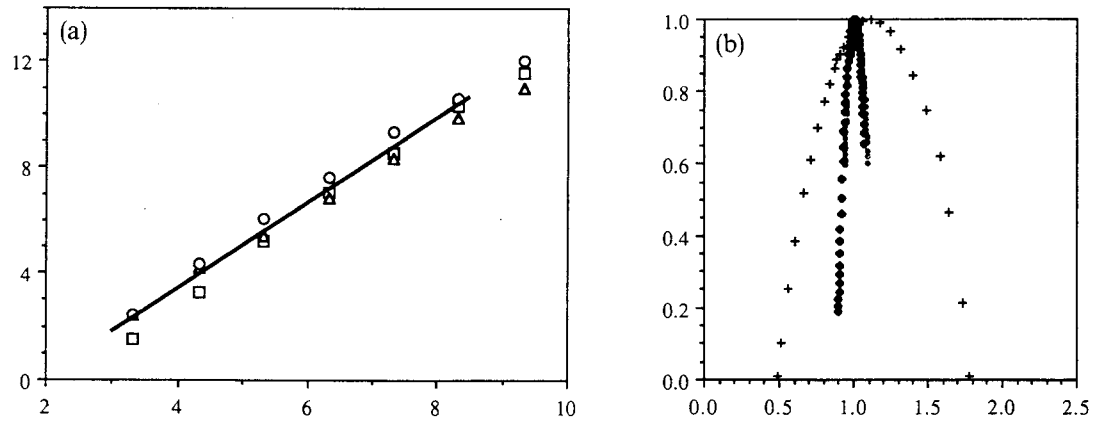

Fig. 2. Fractal properties of the flow: (a) $\log_2 N(\delta)$ versus $\log_2(\delta)$ curves calculated for three velocity components (different symbols). Continuous line refers to linear regression of these curves. (b) $f(\alpha)$ curves, f (vertical axis) versus α (horizontal axis), calculated from the simulated velocity components (given by the black symbols), and for velocity measurements of Meneveau and Sreenivasan (1987) (given by + symbols).

points in space with dimension

$$D_{\text{M.C.}} = 2 + f(\alpha_{\text{M.C.}}) = 3 - |1 - \alpha_0|. \tag{2.14}$$

Meneveau and Sreenivasan (1987) present data which gives $\alpha_0 = 1.12$, $D_{\text{M.C.}} = 2.88$.

Our simulation data produced $\alpha_0 = 1.01$, $D_{\text{M.C.}} = 2.99$. The latter is only slightly different from the theoretical mono-fractal result, which is $\alpha_0 = 1$, and $D_{\text{M.C.}} = 3$. Note that for the mono-fractal (2.13) should be replaced by

$$f(\alpha) = 1, \text{ for } \alpha = \alpha_0$$
$$= 0, \text{ otherwise} \tag{2.15}$$

Thus, in the present model the dissipation is spread over the entire flow domain, since (2.12) is evidently almost a mono-fractal (Fig. 2b).

3. Passive scalar dispersion

3.1. Numerical simulation

In order to simulate the dispersion of a passive scalar, we release 10^4 particles and calculate their path-lines in a frame of reference which moves with the mean flow; these path lines are given by

$$\frac{\mathrm{d}x_m}{\mathrm{d}t} = u_m(x_1, x_2, x_3), \quad m = 1,2,3, \tag{3.1}$$

where u_m are given by (2.12) with the specific data given in Section 2.4.

At the instant of release, $t = 0$, the particle source consisted of 10^4 particles which were randomly scattered within a cube with side 0.5 cm. The cube side was chosen to be between the sizes of the smallest and largest eddies in the flow to reflect inner fluctuation as well as meandering. The integration of the system (3.1) was carried out using a fourth order Runge–Kutta method where a time step $\Delta t = 10^{-4}$ s was chosen to avoid numerical integration errors.

The evolution of a typical cloud of particles, which we call a puff, is demonstrated in Fig. 3, where the puff and its three projections are shown at $t = 0.25, 0.5, 0.75$ and 1 s. Studying the divergence of trajectories of two particles which were very close to each other at $t = 0$, convinced us that the system (3.1) is very sensitive to small changes in the initial conditions which is evident from the convoluted structure of the resulting puffs.

This later observation is supported by the fact that the Lyapunov exponents, calculated according to Wolf et al. (1985), which we have obtained are λ, 0, $-\lambda$; were $\lambda \approx 10\,\text{s}^{-1}$. There are three Lyapunov exponents because the system (3.1) consists of three equations. Any continuous dynamical system, without a fixed point, has at least one zero exponent, corresponding to the slowly changing magnitude of a principal axis tangent to the trajectory. The fact that the sum of the three exponents, in our calculations, is zero is a result of the incompressibility of the flow field (2.2). For comparison, applying the same routine to a flow field generated by a single Taylor–Green vortex gives λ which tends to zero.

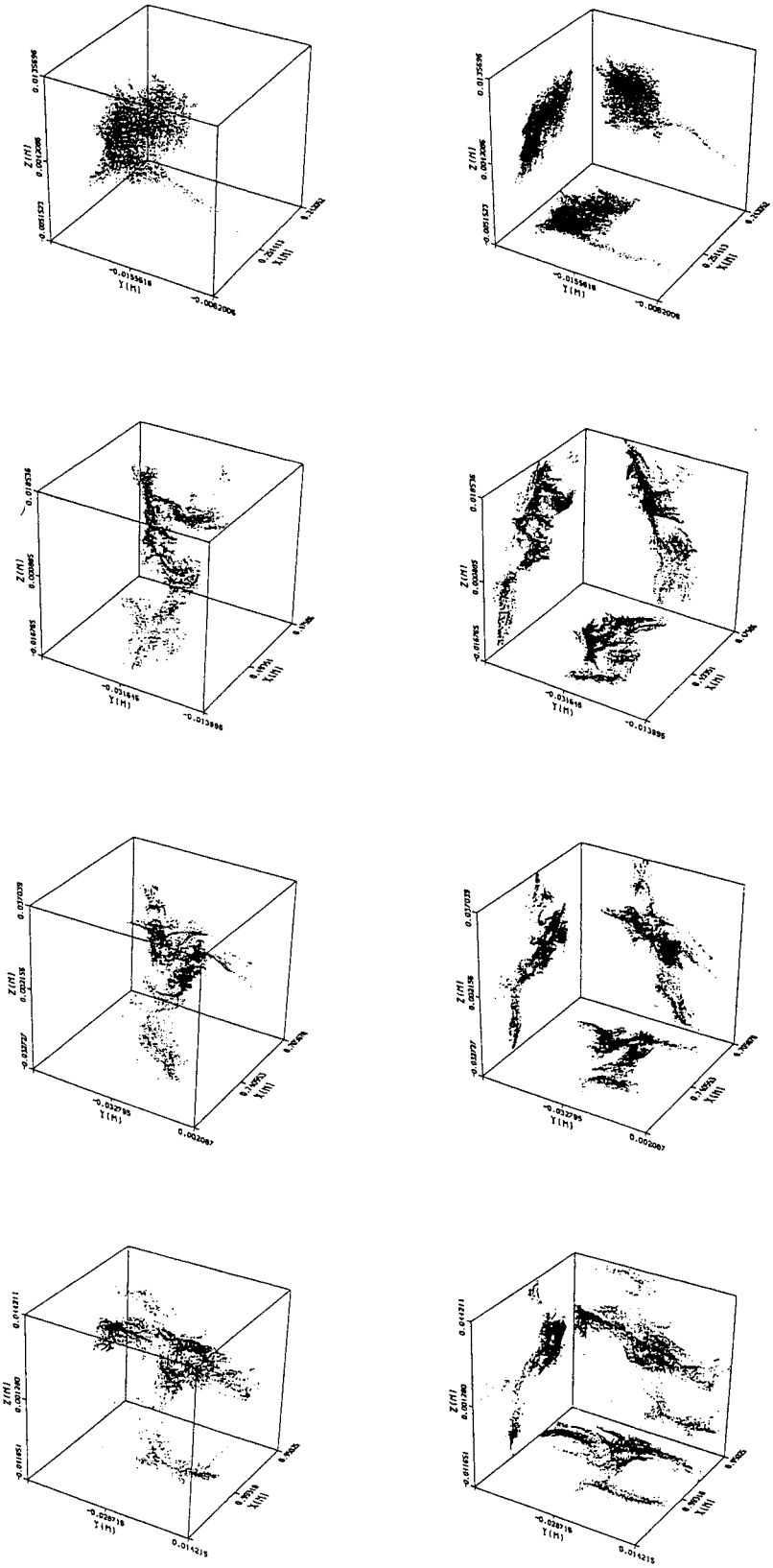

Fig. 3. Blown-up simulated puffs of 10^4 particles (in the left clumn) and their projections (in the right column) for four different instances (from top to bottom) $t = 0.25$, 0.5, 0.75 and 1 s. The magnification factors are 4.5, 2.3, 1.4 and 1, respectively.

3.2. Fractal geometry of the puffs

The box counting algorithm applied to the Y–Z projection of the puff at $t = 1$ s (see Fig. 3) is shown in Fig. 4. At each 'generation' the embedding domain is divided into $2^m \times 2^m$, boxes and the boxes in which one finds at least one particle are 'flagged'. (Fig. 4 includes the $m = 3,4,5$, and 6 generations). The $\log_2$ of number of flagged boxes versus $\log_2$ of the box size is shown in Fig. 5a for the actual puff and its three projections. The box dimension D_{puff} is calculated from the slope of the best straight line passing through the data within upper and lower length scales. The most left edge of the straight lines refers to boxes with size π/k_0 whereas the right edge to boxes of size $\pi/k_0\,\gamma^{N-1}$. The fractal (box counting) dimensions of the puff D_{puff} at different stages of the evolution described in Fig. 3 is given by the open circles in Fig. 5b. As the puff evolves and stretches its fractal dimension reduces from the dimension of the embedding domain 3 (note that the particles are initially randomly distributed in the puff) at $t = 0$ to about 1.67 at $t = 1$ s, which seems to be related to the $D = 5/3$ of the Weierstrass function discussed in Section 2.3. It is believed that the fact that the dimension of the mature puff is less then two is related to their fibrous structure due to stretching and folding.

In Fig. 5b we also show the calculated dimension of the three orthogonal projections of the puff (presented by solid circles) shown in the right column of Fig. 3. In this case the fractal dimension of the projected clouds of particles reduces from 2 at $t = 0$ to about 1.67 at $t = 1$ s, in agreement with the results for the dimension of the puff and the projection theorem given in Falconer (1990). In his comments after theorem 6.2, Falconer concludes: "Thus if F is a subset of $\mathbb{R}^3$, the plane projections of F are, in general, of dimension min $\{2, \dim F\}$".

We have also applied the box counting algorithm to calculate the perimeter dimension of the puffs (sometimes called the scalar interface dimension). Considering Fig. 4 one plots the $\log_2$ of

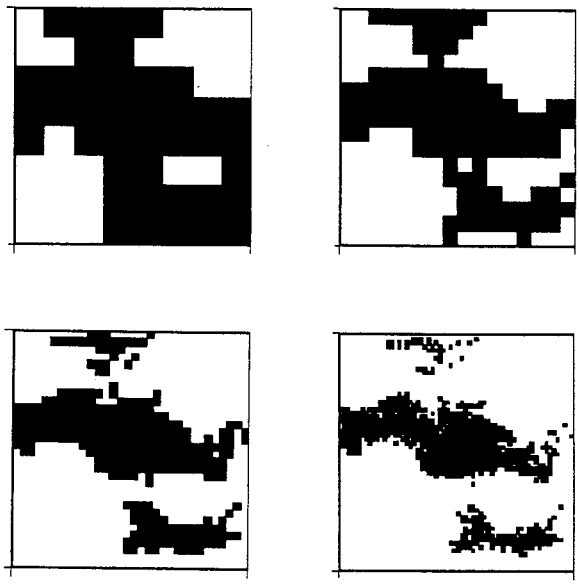

Fig. 4. Box counting algorithm applied to the Y–Z projection of the puff at $t = 1$ s (Fig. 3), for four generations: $m = 3$ (top left), 4 (top right), 5 (bottom left) and 6 (bottom right).

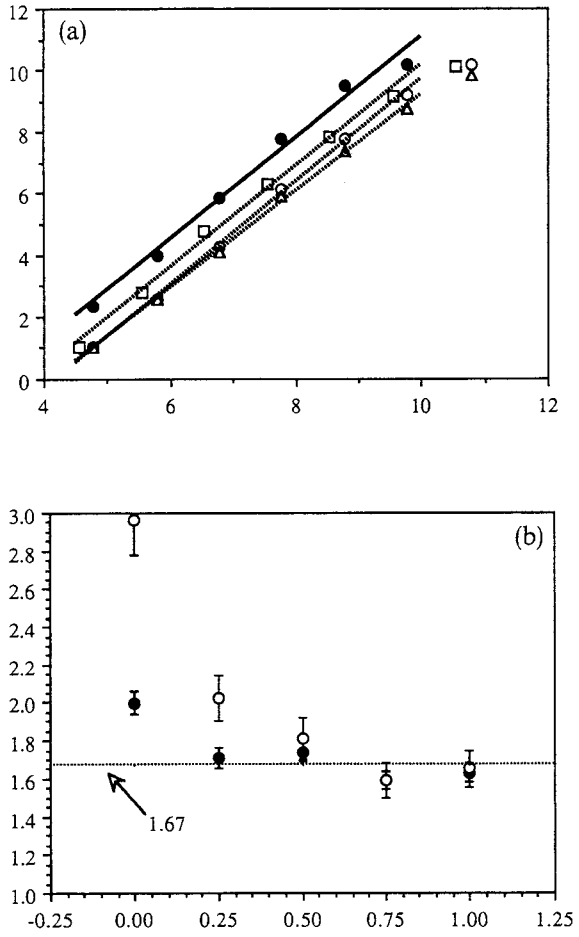

Fig. 5. The dimensions of the puff: (a) $\log_2 N(\delta)$ versus $-\log_2(\delta)$ curves calculated for the puff (●), and for its projections (△,□,○) at $t = 1$ s. (b) Evolution in time t (horizontal axis) of the fractal box dimensions D_{puff} (vertical axis) of the puff (○), and its projections (●).

number of boxes on the perimeter of the puff at a given generation versus $-\log_2$ of box size, where an interface box is a box which has less than eight flagged neighboring boxes (Fig. 6a). As before we use the slope of the straight line in Fig. 6a in a range equivalent to that considered in Fig. 5a to calculate D_{per}. In the present context, the above direct box counting technique used to calculate D_{per}, was found to be more efficient than the known 'perimeter-area relation' technique described in the literature [see Feder, 1988]. The dimension of the perimeter of the projected puffs, D_{per} given in Fig. 6b, increases from 1 at $t = 0$ to about 1.33 at $t > 0.5$ s, comparable to the values obtained for atmospheric clouds. Prasad and Sreenivasan (1990) have found that the boundary of dye-marked regions in turbulent shear flow is a statistically self-similar object with fractal dimension of about 2.35 ± 0.05, which corresponds to a projected boundary with fractal dimension 1.35 ± 0.05.

3.3. *Measurements of integrated concentration*

In Chapter 4, we compare results from the simulation model, with wind tunnel measurements of integrated concentrations (IC) fluctuations across buoyant plumes emitted from a continuous

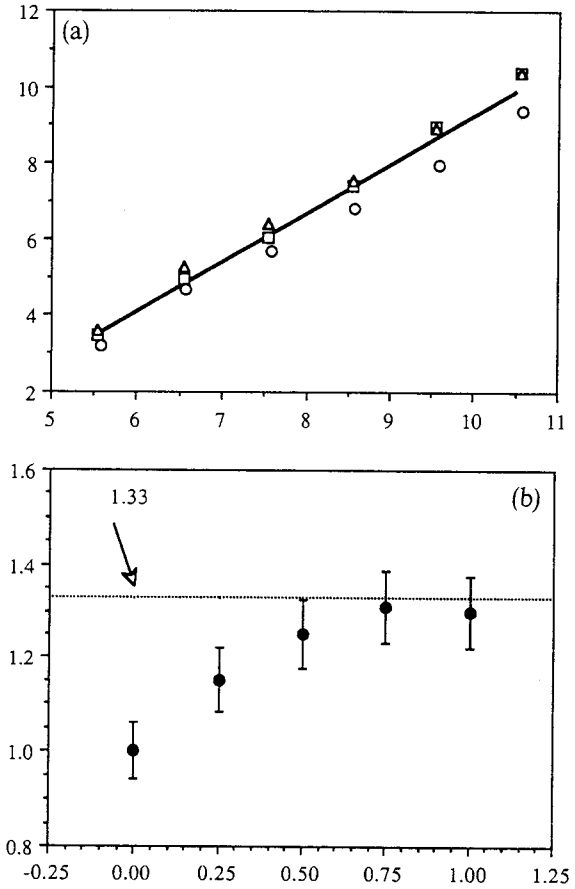

Fig. 6. The dimension of the perimeter of the puff: (a) $\log_2 N(\delta)$ versus $\log_2(\delta)$ curves calculated for the perimeter of three puff projections (△,□,○) at $t = 1$ s. The continuous line refers to the linear regression of these curves. (b) Evolution in time t (horizontal axis) of the fractal box dimension of the perimeter D_{per} (vertical axis) of the projected puff.

point source of a carbon dioxide tracer. IC is defined as

$$IC(x, y, t) = \int_0^\infty C(x, y, z, t)\, dz \tag{3.2}$$

where C is the carbon-dioxide concentration. Measurements were carried out in the Industrial Aerodynamics Wind Tunnel at the Colorado State University (Poreh et. al, 1993). This experimental system works on the principle of absorption of IR radiation across a carbon–dioxide plume.

Measurements of IC were taken at different locations in the down wind direction in the wind tunnel. In the present discussion, we concentrate on analyzing time records of IC fluctuations along the center line of a plume diffusing in a grid generated turbulence configuration (Fig. 7).

A typical measurement record consists of 8×10^3 sampling points sampled at a rate of 300 Hz, which yields a measurement duration of about 840 M/U ($U = 2.4$ m/s is the average wind in the wind tunnel test section and $M = 7.6$ cm is the grid spacing). The measurement resolution, in terms

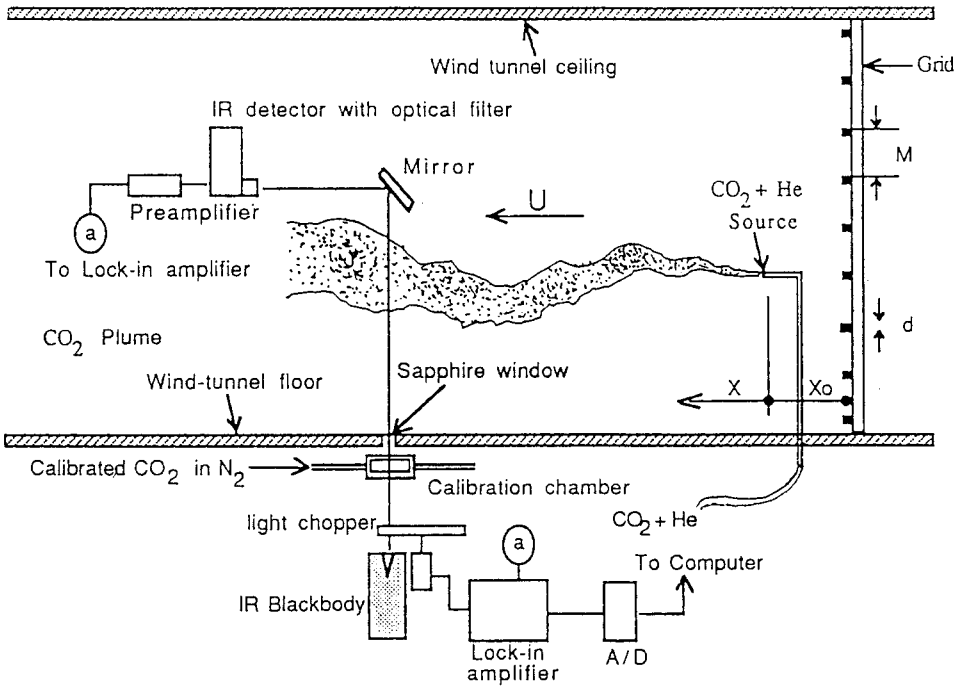

Fig. 7. Schematic description of the experimental setup for measuring integrated concentration in a grid generated turbulence configuration, $M = 7.6$ cm, $d = 1.5$ cm (porosity = 0.64); $U = 2.4$ m/s.

of the down-wind displacement between samples, was 8 mm. Limitations of the experimental setup did not enable to further improve the measurement resolution: The *IR* beam diameter could not be reduced much below its present size (4 mm) and also the sampling frequency could not be increased due to filtering limitations. On the other hand, one should notice that small scale information of point concentration fluctuations is lost anyhow due to integration across the plume. Fortunately the lost effect reduce the impact of resolution limits. Our data analysis experience (Hadad et al., 1993) indicates that the sample size and sampling resolution we have used was large enough to produce significant scaling characterization within scales of interest. Finally the noise to signal ratio of the measurements discussed hereafter was found to be of the order of 0.5 percent.

The situation in the experiment, where a continuous release of the tracer was measured at fixed locations, is basically different from the single release event and detailed spatial distribution which we have in the simulation. To overcome this difference and enable comparison, we generate one dimensional *IC* records from the simulated puffs using a procedure as described below. First, we generate a projection of a puff, similar to those shown in Fig. 3. Second, we divide the embedding large square into a mesh of $2^L \times 2^L$ small squares and count the number of particles which are projected into each of these small squares. We then regard the number of particles in a small square as the *IC* within the specific resolution. The normalized magnitude of *IC* from the projection on the Y–Z plane of the puff at $t = 1$ s for $L = 7$ (which yields a resolution of about 1 mm) is reflected by the height of the vertical shades in Fig. 8a. Finally, we form a one dimensional sequence by scanning the squares, line by line, and retaining only those values which are not zero. A typical outcome is the record shown in Fig. 8b.

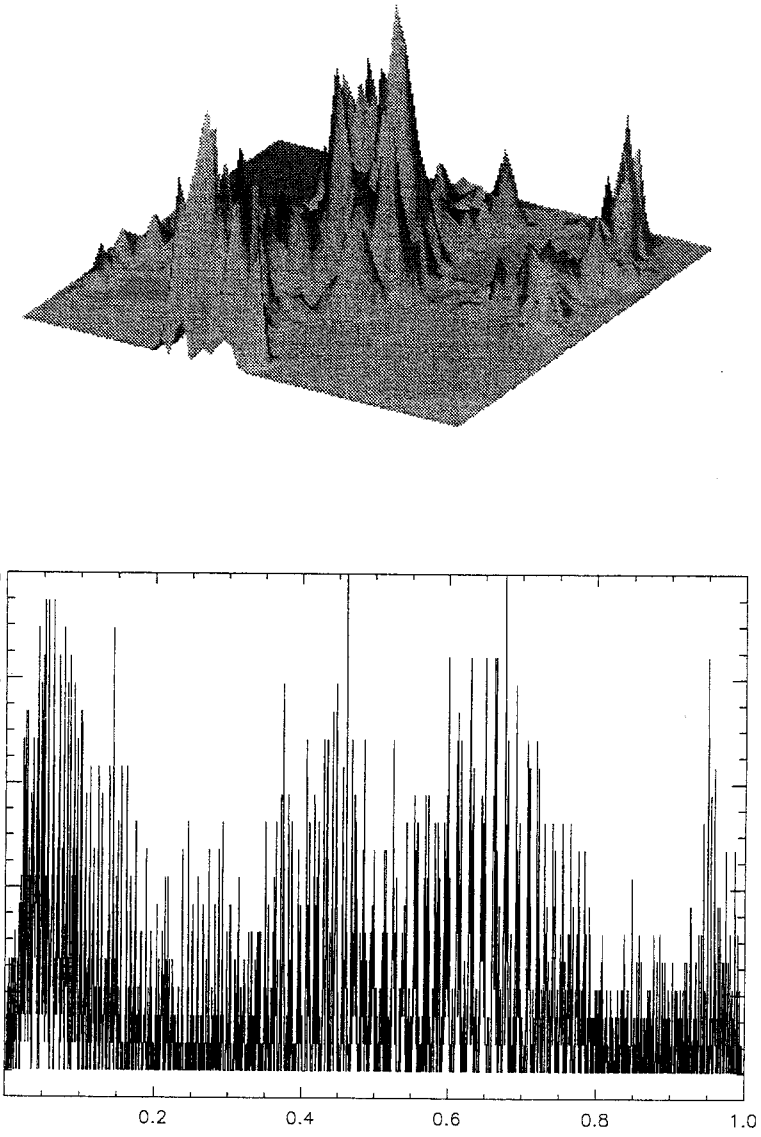

Fig. 8. Generation of simulated integrated concentration record IC (vertical axis) versus $\hat{x}$ (horizontal axis), shown in (b) (bottom), from the planar integrated concentration given in (a) (top).

4. Comparison between simulation and experiments

4.1. *Frozen turbulence hypothesis*

In this chapter, we use a few data analysis techniques in order to compare the simulated integrated- concentration records IC_S with their experimentally measured counterpart IC_M.

The measured records were taken at fixed distance $x = \chi$ from source at $x = 0$, and are functions of the time t; i.e., $IC_M(t, \chi)$. The simulated integrated-concentration records (generated as mentioned in the previous section) were calculated at a few fixed times $t = \tau$ measured from the instant of release $t = 0$, and are a function of some spatial coordinate $\hat{x}$, i.e., $IC_S(\hat{x}, \tau)$.

The frozen turbulence hypothesis allows us to treat the time t in IC_M as equivalent to the distance $\hat{x}$ in IC_S, as long as the puff in the simulation is at about the same stage of development as that of the plume at the measuring station. The stage of development of the simulated puff is governed by the dimensionless parameter $\xi_S = \tau(\sigma_u)/(2\pi/k_0)$, whereas its counterpart for the measurements is $\xi_M = \chi I(2\pi/k_0)$.

4.2. *Fractal and multifractal analyses*

In Fig. 9 we show the fractal dimension D_{IC} of the IC records at different stages of development ξ. The box counting technique applied here is similar to that mentioned regarding D_b calculations from velocity records (Fig. 2), and the length scale range at which slopes are estimated is as before (Figs. 5 and 6).

The open circles show the simulated results, and the solid circles represent the experimental data. If we omit the first simulated point (where the puff is still premature), then all other points, experimental and simulated, give $D_{IC} \approx 1.62 \pm 0.05$.

In Figs. 10a and 10b, we present the multifractal singularity spectrum $F(\alpha)$ and the dissipation singularity spectrum $f(\alpha)$, respectively. The multifractal singularity spectrum provides information about the distribution of the Lipschitz–Holder exponent α for $y(x)$, the graphs of these records. A certain value of α is related to the local behaviour of the graph; i.e. to the range of y, denoted by Δy, within an interval Δx, which is assumed to be proportional to Δx^{α}. $F(\alpha)$ is the fractal dimension of the dust (infinite collection of points on the x axis) which supports a specific Lipschitz–Holder exponent α.

To obtain the dissipation singularity spectrum $f(\alpha)$, we first calculate a new function which is proportional to what is the so-called "dissipation". This function, say $z(x)$ is calculated by summing the squares of the IC gradients: $z(x) = \Sigma \Delta y^2$. Then we analyze $z(x)$ as we did for $y(x)$. The method of derivation of these spectra and their mathematical meaning is outlined in the Appendix. The simulated results are for $\xi_S = 0.60$ and are marked by ▲, whereas the measured curves are for $\xi_M = 0.71$ and we have marked them by ●. The general agreement between theory and experiment

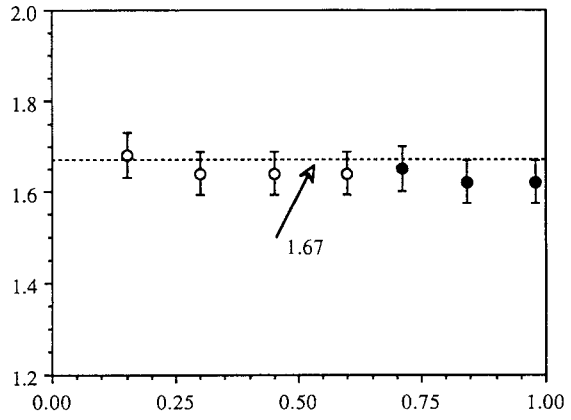

Fig. 9. Fractal dimension of integrated-concentration records, D_{IC} vertical axis versus t (horizontal axis): simulation (○), measurements (●).

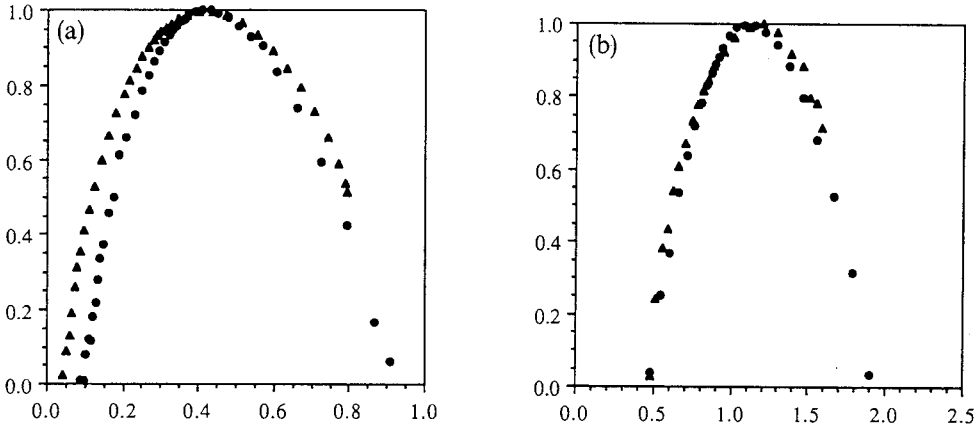

Fig. 10. Comparison simulation (▲) with measurements (●). (a) Multifractal singularity spectrum F (vertical axis) versus α (horizontal axis), (b) Dissipation singularity spectrum f (vertical axis) versus α (horizontal axis).

is more than fair for $F(\alpha)$ and rather good for the dissipation singularity spectrum $f(\alpha)$ considering the limitations of the flow model (Fig. 2b) and the relatively low number of particles involved in the simulation. Further, in a previous paper (Hadad et al., 1993) we have showed that $f(\alpha)$ curves calculated from IC time records (such as the one showed in Fig. 10b) and from turbulent velocity time records (Meneveau and Sreenivasan, 1987) are rather similar. This indicates that the proposed simulation model captures the structure of the singular behavior of the measured process in great detail.

4.3. *Spectral analysis*

Spectral analysis is one of the most frequently used techniques in analyzing and presenting experimental (physical or numerical) data. It is common knowledge in the field that substantial averaging is needed if one wants to present rather smooth spectral shapes. The question which we are trying to raise in the present section refers to the information lost by the process of averaging.

In Figs. 11a and 11b we show two possible presentations of the power spectrum of the simulated integrated concentration, IC_s. Fig. 11b is the "raw" result of applying a F.F.T. on a record with 1024 data points. Whereas each symbol in Fig. 11a is an average of 18 values obtained from 18 different realizations of the spectrum such as that given in Fig. 11b. The averaging technique is common practice in spectral analysis and it enables to recover general trends, such as the straight line with slope $= -5/3$ shown in Fig. 11a. However, by doing so, one clearly loses the information about the singularity structure of the power spectrum itself.

If we analyze crude spectra like the one in Fig. 11b for their multifractal structure in wave-number space (see Appendix A.3), we obtain what one may call the Spectral Singularity Spectrum $\varphi(\alpha)$, shown in Fig. 12. Here we have treated the graph of the accumulated power spectrum, which has a form of a "Devil's staircase". Thus $\varphi(\alpha)$ gives information on the intensity (characterized by α), and frequency (given by $\varphi(\alpha)$) of the jumps in the staircase. From Fig. 12 we see that the distribution of singularities in the power spectrum of IC_S(at $\xi_s = 0.60$) is fairly similar to the distribution of singularities of the measured counterpart IC_M(at $\xi_M = 0.71$). The spectral singularity spectrum is

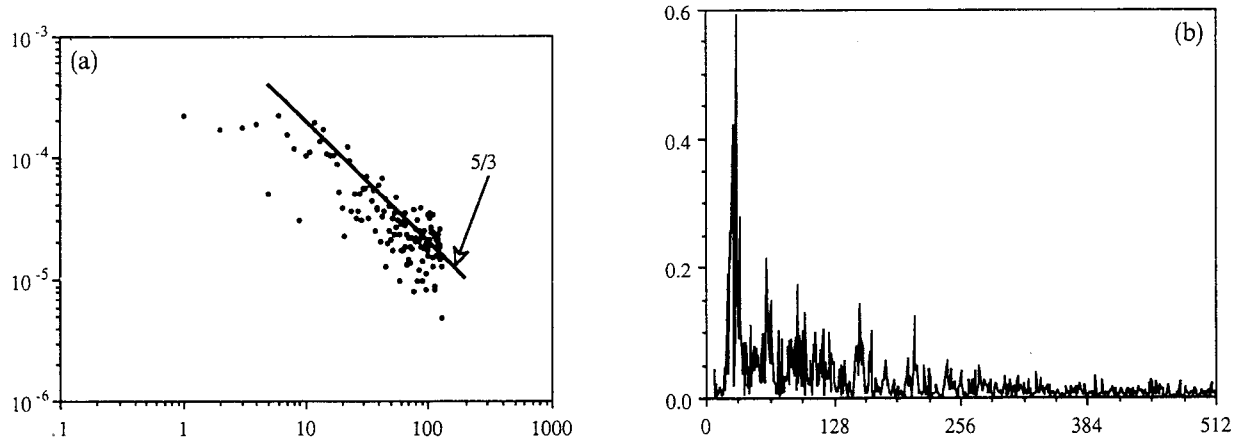

Fig. 11. Power spectrum of the simulated integrated-concentration records: (a) Average of 18 realizations similar to the one shown in b. (b) Crude spectrum

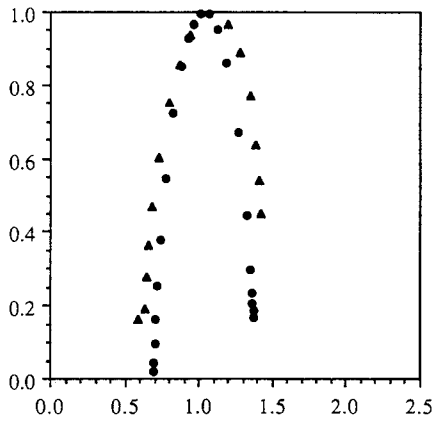

Fig. 12. Comparison of simulated (▲) and measured (●) spectral singularity spectrum, φ (vertical axis) versus α (horizontal axis).

somewhat narrower than the multifractal singularity spectrum $F(\alpha)$. However we believe its spread is wide enough, not to be attributed to uncertainties.

5. Conclusions

The authors of this paper share the belief that the presently available mathematical tools are not adequate for a complete analytical treatment of turbulent flow fields, even under the simplifying assumption of homogeneity.

Thus, we think that one should be rather content with a not too complicated simulation model which captures many of the known features of turbulent flow fields. The turbulent fluctuation model which we developed in Chapter 2 fulfills this requirement. In particular, it 'gives life' to the notion of turbulent eddies, which everybody uses but few 'dare' to define. Our model for turbulent

fluctuations satisfies the most crucial requirements, such as: (i) continuity, (ii) Kolmogorov's inertial range law, and (iii) scaling properties.

The main drawback of our model is that it brings the dynamics in only through the rear door, i.e. by utilizing Kolmogorov's spectrum. Therefore, we think that it falls short from providing a new theoretical basis to study turbulence and eddies.

However, the detailed analysis of the evolution of a particle cloud emitted into the model flow field described in Chapter 3, and the comparisons with experimental data in Chapter 4, strengthen our view that the model turbulent field given by (2.12) provides a reliable practical tool to simulate turbulence. Our calculations show that the experimentally measured integrated concentration and its simulated counterpart are almost undistinguishable under a series of rather carefully designed tests.

Acknowledgements

Michael Stiassnie completed part of this work at the Department of Engineering Mathematics, University of Bristol. He acknowledges the support of the Science and Engineering Research Council Grant No: GR/H94894 - S23603. He is also grateful to Professor S.J. Hogan and the staff of the Department for their hospitality.

Appendix. On three different singularity spectra

A.1. F(α), multifractal singularity spectrum

We start with a set of points which is a sampling of some continuous, bounded, single-valued function $y(x)$, in the domain $[0, 1]$. We divide the x-axis in the domain $[0, 1]$ into n equal segments δ, $n = \delta^{-1}$, and denote $x_i = i\delta$; $i = 0, 1, \ldots, n$.

The number of δ by δ boxes which is needed to cover $y(x)$ in the domain between x_i and $x_i + \delta$ is $\Delta(x_i, \delta)/\delta$, where

$$\Delta(x_i, \delta) = y_{\max}(x, \delta) - y_{\min}(x, \delta), \quad x_i \leq \times \leq x_i + \delta. \tag{A.1}$$

Thus, the total number of boxes $N(\delta)$ which is needed to completely cover $y(x)$ is $\sum_{i=0}^{n-1} \Delta(x_i, \delta)/\delta$. The box-counting (fractal) dimension D_b of $y(x)$ is defined and exists only when the following measure M is finite:

$$M = \lim_{\delta \to 0} \delta^{D_b - 1} \sum_{i=0}^{n-1} \Delta(x_i, \delta). \tag{A.2}$$

D_b is obtained from the slope of the graph of $\log \sum_{i=0}^{n-1} \Delta(x_i, \delta)$ plotted as a function of $\log(1/\delta)$, for small enough values of δ.

The local behavior of the function $y(x)$, in terms of its Lipschitz–Holder (L–H) exponent α, is represented by

$$\Delta(x_i, \delta) \propto \delta^{\alpha}, \tag{A.3}$$

where α determines the singularity strength, and $(1-\alpha)$ sets the rate by which the derivative tends to infinity. For turbulent data one would expect $y(x)$ to have different values of α at different locations. Actually, $y(x)$ is characterized by a union of an infinite number of subsets each related to a typical singularity α and supported by dust on $[0,1]$ with a fractal dimension F_α. The $F(\alpha)$ curve is the mulifractal singularity spectrum, which we want to find.

The number of boxes which is needed to cover a subset with L–H exponent between α and $\alpha + \mathrm{d}\alpha$ is

$$N(\alpha, \delta) \propto \delta^{-F(\alpha)}\,\mathrm{d}\alpha. \tag{A.4}$$

A more general measure than that in (A.2) is the q-measure of the set

$$M_q = \lim_{\delta \to 0} \delta^{\tau(q)} \sum_{i=0}^{n-1} \mu_i^q, \tag{A.5}$$

where $\tau(q)$ are sometimes called the 'mass exponents' and μ_i, which denotes the relative weight in the ith segments, is defined as

$$\mu_i = \Delta(x_i, \delta)\left(\sum_{i=0}^{n-1} \Delta(x_i, \delta)\right)^{-1}. \tag{A.6}$$

Note that one can compute $\sum_{i=0}^{n-1} \mu_i^q$ for decreasing values of δ. The plot of $\log \sum_{i=0}^{n-1} \mu_i^q$ against $\log (1/\delta)$ serves to obtain $\tau(q)$, for given q.

From Eqs. (A.2), (A.3) and (A.6), we get an expression for the relative weight in a segment as a function of its L–H exponent and of the box-counting dimension:

$$\mu(\alpha, \delta) \propto \delta^{\alpha + D_\mathrm{b} - 1}. \tag{A.7}$$

Using Eqs. (A.4) and (A.7) we can write the q-measure in the form

$$M_q \propto \lim_{\delta \to 0} \int_0^\infty \mathrm{d}\alpha^{-F(\alpha) + (\alpha + D_\mathrm{b} - 1)q + \tau(q)}. \tag{A.8}$$

The integral in Eq. (A.8) is calculated by the steepest descent approximation. In the limit of small δ this integral is dominated by

$$M_q \propto \delta^{-F(\alpha) + (\alpha + D_\mathrm{b} - 1)q + \tau(q)}, \quad \alpha = \alpha(q), \tag{A.9}$$

where α in Eq. (A.9) is the solution of $F'(\alpha) = q$, provided that $F''(\alpha) < 0$. The measure M_q in Eq. (A.9) is finite only when

$$F(\alpha) = (\alpha + D_\mathrm{b} - 1)q + \tau(q). \tag{A.10a}$$

Taking the derivative of Eq. (A.10a) with respect to q, we find

$$\alpha = 1 - D_\mathrm{b} - \mathrm{d}\tau(q)/\mathrm{d}q. \tag{A.10b}$$

The couple of Eqs. (A.10a) and (A.10b) enables to calculate the multifractal singularity spectrum $F(\alpha)$, when the mass exponents curve $\tau(q)$ and the fractal dimension D_b of the set are known from, say, measured or simulation data.

A.2. $f(\alpha)$, the dissipation singularity spectrum

The original function $y(x)$ is first transformed as follows:

$$z(x) = \int_0^x \left(\frac{dy}{dx}\right)^2 dx. \tag{A.11}$$

Then we apply the same procedure as outlined in Eqs. (A.5)–(A.10) on $z(x)$. For this case, Eq. (A.2) yields $D_b = 1$, and Eqs. (A.10a) and (A.10b) reduce to the somewhat more known form

$$f(\alpha) = \alpha q + \tau(q), \tag{A.12a}$$

$$\alpha = -d\tau(q)/dq. \tag{A.12b}$$

If one thinks about the original data $y(x$ as velocity or concentration records, then $z(x)$ may be regarded as related to the dissipation of energy or of the scalar, respectively.

A.3. $\varphi(\alpha)$, the spectral singularity spectrum

In this case we first calculate the accumulated power spectrum of the function $y(x)$:

$$w(k_j) = \sum_{n=1}^{j} \left| \int_0^1 y(x) \exp(2\pi i n x)\, dx \right|^2, \quad k_j = 2\pi j, \quad j = 1,2, \ldots . \tag{A.13}$$

Then we use again Eqs. (A.5)–(A.10), replacing $y(x)$ by $w(k)$. Here, as for the dissipation singularily spectrum $D_b = 1$.

This type of analysis sheds light on the nature of the rather spiky structure of power spectra.

References

Batchelor, G.K. (1970) *The Theory of Homogeneous Turbulence* (Cambridge University Press).

Berry, M.V. and Z.V. Lewis, (1980) On the Weierstrass-Madelbrot Fractal Function, *Proc. R. Soc. Lond. A 360*, 459–484.

Brachet, M.E., D.I. Meiron, S.A. Orszag, B.G. Nickel, R.H. Morf and U. Frisch (1983) Small-scale Structure of the Taylor-Green Vortex, *J. Fluid Mech. 30*, 411–452.

Falconer, K. (1990) *Fractal Geometry, Mathematical Foundations and Applications* (Wiley).

Feder, J. (1988) *Fractals* (Plenum Press, New York).

Feller, W. (1971) *An Introduction to Probability Theory and Its Applications*, (Wiley).

Fung, J.C.H., J.C.R. Hunt, N.A. Malik and R.J. Perkins (1992) Kinematic Simulation of Homogeneous Turbulence by Unsteady Random Fourier Modes, *J. Fluid Mech. 236*, 281–318.

Halsey, T.C., M.H. Jensen, L.P. Kadanoff I. Procaccia and B.I. Shraiman (1986) Fractal Measures and Their Singularities: The Characterization of Strange Sets, *Phys. Rev. A 33*, 1141–51.

Hadad, A., M. Stiassnie, M. Poreh and J.E. Cermak (1993), Fractal Aspects of Vertical Integrated Concentrations in Plumes, *Bound. Layer Meteor. 62*, 291–302.

Humphrey, J.A.C., C.A. Schuler and B. Rubinsky (1992) On the Use of the Weierstrass-Mandelbrot Function to Describe the Fractal Component of Turbulent Velocity, *Fluid Dynamics Research 9*, 81–95.

Hunt, J.C.R. (1985) Turbulent Diffusion from Sources in Complex Flows. *Annu. Rev. Fluid Mech. 17*, 447–485.

Jimenez, J., A.A. Wray, P.G. Saffman and R.S. Rogallo (1993) The Structure of Intense Vorticity in Isotropic Turbulence, *J. Fluid Mech. 255*, 65–90.

Kinsman, B. (1965) *Wind Waves, Their Generation and Propagation on the Ocean Surface*, (Prentice-Hall).

Kolmogorov, A.N. (1941) Local Structure of Turbulence in an Incompressible Liquid for Very Large Reynolds Numbers, *C.R. Acad. Sci. 30*, 299–301.

Meneveau, C. and K.R. Sreenivasan (1987) The Multifractal Spectrum of the Dissipation Field in Turbulent Flows, *Nucl. Phys. B. 2*, 49–76.

Osborne, A.R. and R. Caponio (1990) Fractal Trajectories and Anomalous Diffusion for Chaotic Particle Motions in 2D Turbulence, *Phys. Rev. Lett 64*, 1733–1736.

Osborne, A.R. and A. Provenzale (1989) Finite Correlation Dimension for Stochastic Systems with Power-law Spectra, *Physica D 35*, 357–381.

Poreh, M., A. Hadad and J.E. Cermak (1993) Fluctuations of Line Integrated Concentrations Across Plumes Diffusing in Grid Generated Turbulence and in Shear Flows, *Bound.-Layer Meteor. 62*, 247–267.

Prasad, R.R., C. Meneveau, and K.R. Sreenivasan (1988) Multifractal Nature of the Dissipation Field of Passive Scalars in Fully Turbulent Flows, *Amer. Phys. Soc. 61*, 74–77.

Prasad, R.R. and K.R. Sreenivasan (1990) Quantitative Three-Dimensional Imaging and the Structure of Passive Scalars Fields in Fully Turbulent Flows, *J. Fluid Mech. 216*, 1–34.

Rice, S. (1954) *Mathematical Analysis of Random Noise, in Noise and Stochastic Processes* (ed. N. Wax, (Dover Publications).

Sreenivasan, K.R. (1991) Fractals and Multifractals in Fluid Turbulence, *Annu. Rev. Fluid Mech. 23*, 539–600.

Sreenivasan, K.R. and A Juneja, (1993) Fractal Dimensions of Time Series in Turbulent Flows, submitted for publication.

Stiassnie, M., Y. Agnon and L. Shemer (1991) Fractal Dimensions of Random Water Surfaces, *Physica D. 47*, 341–352.

Taylor, G.I. and A.E. Green (1937) Mechanism of the Production of Small Eddies from Large Ones, *Proc. R. Soc. London, A 158*, 499–521.

Wolf, A., J.B. Swift, H.L. Swinney and J.A. Vastano (1985) Determining Lyapunov Exponents from a Time Series, *Physica D 16*, 285–317.